

ARTICLE

Open Access

Undoped tin dioxide transparent electrodes for efficient and cost-effective indoor organic photovoltaics (*SnO₂ electrode for indoor organic photovoltaics*)

Jung-Hoon Lee¹, Young-Jun You², Muhammad Ahsan Saeed², Sang Hyeon Kim³, Su-Hwan Choi⁴, Sungmin Kim³, Sae Youn Lee⁵, Jin-Seong Park¹ and Jae Won Shim³

Abstract

Indoor organic photovoltaics (OPVs) are currently being investigated for small-scale energy generation from artificial light sources to power small electronic devices. Despite recent progress in increasing the power conversion efficiency (PCE) of indoor OPVs, the widespread use of expensive indium tin oxide (ITO) as a transparent conducting electrode (TCE) leads to long energy payback times. This study provides a novel and comprehensive description of low-temperature atomic layer deposition (ALD)-processed indium-free tin dioxide (SnO₂) films as inexpensive and efficient TCEs for indoor OPVs. These highly conformal and defect-free ALD-fabricated SnO₂ films are applied to a poly(3-hexylthiophene):indene-C₆₀ bisadduct-based OPV system. Under 1 sun illumination, an OPV with an SnO₂ TCE exhibits limited operational capacity because of the high sheet resistance (~98 Ω sq⁻¹) of the SnO₂ layers. However, under a light-emitting diode (LED) lamp with a luminance of 1000 lx, the series resistance, which is related to the sheet resistance, has a marginal effect on the performance of the indoor OPV system, showing a PCE of 14.6 ± 0.3%. A reference OPV with an ITO TCE has a slightly lower PCE of 13.3 ± 0.8% under the same LED conditions. These results suggest that SnO₂ TCEs can be efficient and cost-effective replacements for ITO TCEs in indoor OPV systems.

Introduction

Recently, semipermanent indoor energy harvesting systems have been increasingly studied for powering low-power indoor electronic devices, such as sensor network nodes used in the “Internet of Things” technology platform¹. Regarding indoor energy harvesting, the use of thermoelectric, piezoelectric, and photovoltaic (PV) devices show the most promise. Among them, PV harvesters are considered particularly suitable for indoor use due to their high power conversion efficiency (PCE) and

the ability to harvest energy from indoor lighting^{2–4}. To date, PV systems have been fabricated using photoactive materials, such as silicon, gallium arsenide, copper indium gallium selenide, organics, perovskites, and quantum dots^{1–5}. In particular, organic PV (OPV) systems are relatively effective in dim indoor lighting with various output spectra because of their excellent light absorption properties at low light intensities and their adjustable optical bandgap⁵. In addition, OPV systems are the preferred indoor energy conversion option due to their deformability, aesthetic advantages (large variety of cell colors), and less harmful environmental impact^{6–8}. In a recent report, a record PCE of ~28% was obtained using an OPV system under a 1000 lx fluorescent lamp with benzodithiophene terthiophene rhodamine [6,6]:phenyl C₇₁-butyric acid methyl ester photoactive layers⁵.

Correspondence: Jin-Seong Park (jsparklime@hanyang.ac.kr) or Jae Won Shim (jwshim19@korea.ac.kr)

¹Division of Materials Science and Engineering, Hanyang University, Seoul, Republic of Korea

²Division of Electronics and Electrical Engineering, Dongguk University, Seoul, Republic of Korea

Full list of author information is available at the end of the article

© The Author(s) 2021



Open Access This article is licensed under a Creative Commons Attribution 4.0 International License, which permits use, sharing, adaptation, distribution and reproduction in any medium or format, as long as you give appropriate credit to the original author(s) and the source, provide a link to the Creative Commons license, and indicate if changes were made. The images or other third party material in this article are included in the article's Creative Commons license, unless indicated otherwise in a credit line to the material. If material is not included in the article's Creative Commons license and your intended use is not permitted by statutory regulation or exceeds the permitted use, you will need to obtain permission directly from the copyright holder. To view a copy of this license, visit <http://creativecommons.org/licenses/by/4.0/>.

Regarding the indoor operation of OPVs, conventional approaches that are used for outdoor OPV systems need to be modified because of the differences between the indoor and outdoor output spectra and incident light intensities⁹. Under dim indoor conditions, an OPV system produces fewer photons; therefore, the losses due to series (or sheet) resistance must be minimized in indoor OPV systems. Minimizing optical loss, suppressing leakage current, and providing optimum spectrum matching between the absorption spectral range of the photoactive layers and the output spectra of the indoor light source are crucial for the efficient indoor performance of OPVs^{10,11}. Transparent conducting electrodes (TCEs) play a major role in indoor OPV systems, as most indoor performance requirements are functions of the properties of the TCE¹¹.

In general, materials that exhibit high conductivity and transparency are important for fabricating TCEs. Tin-doped indium oxide (ITO) ($\text{In}_2\text{O}_3:\text{SnO}_2 = 90:10\text{--}95:5$), containing outstanding electrical and optical properties, has the largest market share in organic optoelectronic devices, despite the high costs associated with indium, which is a relatively rare element^{12,13}. However, TCEs with moderate conductivity values may be better suited for the application of OPV devices under dim indoor light conditions. In a recent report, we introduced undoped zinc oxide and ultrathin ITO as new types of TCEs for indoor OPV systems¹⁴. The results of our study indicated that pure tin dioxide (SnO_2) was a promising TCE material for indoor applications. Although the use of SnO_2 in outdoor OPV systems remains challenging owing to its poor electrical properties (necessitating additional doping with antimony¹⁵, fluorine^{15,16}, or niobium¹⁷), its optical and electrochemical properties (work function (WF) values of 4.3–4.7 eV) and chemical resistance¹⁸ appear to be suitable for indoor systems.

In this paper, we discuss a proof-of-concept demonstration of an indoor OPV system using an SnO_2 TCE fabricated via atomic layer deposition (ALD) with an *N,N'*-tert-butyl-1,1-dimethylethylenediamine stannylene (II) precursor; this system has never been used before in OPV TCE applications. The ALD process is based on a self-limiting surface reaction, which produces uniform and conformal thin films with precisely controlled thicknesses at relatively low temperatures. These properties are particularly advantageous for developing TCEs with low leakage current for indoor OPVs. Owing to the lack of appropriate tin precursors for the ALD method, SnO_2 thin films are most often fabricated via physical vapor deposition (PVD) techniques, such as pulsed laser deposition^{16,19} and sputtering^{20,21}. We investigate the effect of annealing temperature on the structural, morphological, optical, electrochemical, and electrical properties of the ALD-synthesized SnO_2 films. The performance of the SnO_2 TCE is verified by using a poly(3-hexylthiophene) (P3HT):indene- C_{60} bisadduct (ICBA)-OPV system under both outdoor and

indoor conditions and compared with those of reference devices containing commercially available ITO TCEs. The exclusion of indium from the TCE is expected to result in a price reduction of ~20%, which substantially reduces the payback time of a PV system.

Experimental methods

Fabrication of transparent conducting electrode

SnO_2 films were deposited on silicon, SiO_2 , ITO glass, and glass substrates, depending on the intended purpose in a growth-temperature range of 100–250 °C using 6-inch lateral gas flux thermal ALD (Lucida D-100, NCD). The chamber pressure was set to 300 mTorr with 50 sccm of nitrogen (N_2 , 99.999%) purge gas. The sequential process of precursor dose/purge/reactant dose/purge was applied as the standard ALD process. The purge time was 10 s for all ALD processes. *N,N'*-tert-butyl-1,1-dimethylethylenediamine stannylene (II) was used as the tin precursor for the growth of SnO_2 thin films. The precursor was stored in a stainless-steel canister, the precursor temperature was varied from 30–60 °C to control the vapor pressure, and N_2 was used as the carrier gas. Ozone was employed as the reactant. Ozone was carried to the reactor at 500 sccm (ozone concentration was set to ~13%). ALD was self-limiting depending on the precursor, reactant dose, and ALD window, as shown in the Supplementary Information (Fig. S1).

Thin film characterization

The thickness, refractive index, and extinction coefficient of the thin films were measured by a spectroscopic ellipsometer (SE, UV-FMS, Ellipso Technology, National Nanofabrication Center). The crystallinities of SnO_2 were revealed by XRD (Rigaku, Smartlab) with the 2-theta method at a glancing angle of 3°. The surface morphology of the thin films was obtained with atomic force microscopy (ParkSystem, XE-100). The atomic composition ratio was investigated using XPS with a theta probe (Thermo Fisher Scientific Co). Ultraviolet-visible light spectrophotometry (Lambda 650 S, Perkin Elmer) was used to measure the transmittance and absorbance of the thin films. The optical bandgap was extracted using the Tauc plot extrapolation method.²⁹

Solution preparation

PEIE (80% ethoxylated, $M_w \sim 70,000$ g/mol, 35–40 wt.% water, Aldrich, St. Louis, MO, U.S.A.) was diluted with 2-methoxyethanol (Aldrich, St. Louis, MO, U.S.A) to a concentration of 0.2 wt.% and stirred overnight in ambient air. A solution of P3HT (4002E, Rieke Metals, Lincoln, NE, U.S.A.):ICBA (Luminescence Technology Corp., New Taipei City, Taiwan) was prepared in 1,2-dichlorobenzene (Aldrich, St. Louis, MO, U.S.A.) at a weight ratio of 1:1 (P3HT:ICBA), and a total P3HT:ICBA concentration of 40 mg/ml. The P3HT:ICBA solution was kept and stirred overnight in a N_2 -filled glove box at 70 °C.

Device fabrication

Prepatterned and ITO-coated glass panels (AMG, Republic of Korea) with a sheet resistivity of $10 \Omega\text{-sq}^{-1}$ were used as substrates for the reference device and the SnO_2 TCEs. All substrates were cleaned in an ultrasonic bath of Liqui-Nox phosphate-free liquid detergent (Alconox, Inc., White Plains, NY, U.S.A.), rinsed with deionized (DI) water, and then cleaned in sequential ultrasonic baths of DI water, acetone, and 2-propanol. Nitrogen was used to dry the substrates after each bath. The substrates were then ultrasonicated in 2-propanol for 10 min and dried with nitrogen. The 5.6-nm-thick PEIE layer was spin-cast onto the substrates in air at a speed of 5000 rpm for 1 min by filtering the PEIE solution through a 0.2- μm PTFE filter. The PEIE-coated substrates were dried in air on a hot plate at a temperature of 110°C for 10 min. They were then loaded into a nitrogen-filled glove box. Approximately 150-nm-thick films of P3HT:ICBA were deposited by spin-coating at 800 rpm for 30 s by filtering the solution through a 0.2- μm PTFE filter and annealed at 150°C for 10 min in a N_2 atmosphere. A cross-section of the devices was analyzed using field-emission scanning electron microscopy (S-4800, Hitachi) with an accelerating voltage of 15.0 kV. The samples were then loaded into a vacuum thermal evaporation system (Daedong High Tech, Republic of Korea) connected to a N_2 -filled glove box, and a 10-nm-thick layer of MoO_x was deposited through a shadow mask at 0.1–0.15 nm/s and a base pressure of $\sim 4.5 \times 10^{-8}$ Torr. Without breaking the vacuum, a 150-nm-thick silver layer was deposited through the previously used shadow mask at 0.1–0.2 nm/s and a base pressure of $\sim 4.5 \times 10^{-8}$ Torr.

Device characterization

Current density–voltage (J – V) characteristics in the dark and under illumination were measured by a source meter (2401, Keithley Instruments, Cleveland, OH) and controlled by a K730 program (McScience, Republic of Korea). An AM 1.5 G solar simulator (McScience, Republic of Korea) with an irradiance of 100 mW/cm^2 was used as the light source. An LED lamp (SLS LED100, color temperature from 3000 K to 3500 K, McScience, Republic of Korea) with an irradiation of $0.28 \text{ mW}\cdot\text{cm}^{-2}$ (at 1000 lx) was used for the indoor light. The luminance and irradiance of the LED lamp were measured by a Sun spectroradiometer (S-2441C, HIDAMARI mini II, Japan). The external quantum efficiency (EQE) was evaluated by using an incident photo-to-current efficiency measurement system (ORIEL IQE 200 system, U.S.A.). The active area of the OPVs was $\sim 0.1 \text{ cm}^2$ for each device, as determined by optical microscopy.

Finite-difference time-domain simulation

Optical density distributions of the SnO_2 films with varying thicknesses and the reference ITO films were simulated using Lumerical Solutions software (Vancouver, Canada).

The optical information of the material, expressed as n and k values, was prepared in the simulation, and 2-dimensional device structures were designed with those values. The simulation domain conditions were the periodic boundary conditions for the x and y axes, and the perfectly matched layer condition was used for the z axis. An overall mesh size of 3 nm was chosen to produce a fine-scaled design. The z and x directions were the directions of the incident light and the polarization, respectively. The absorption was estimated by calculating the frequency-domain field and power monitor. Before calculating the current density, the plane wave source, which included a continuous wave, was placed below the bottom electrode. We used SnO_2 and ITO as bottom electrodes. The ideal current density was computed by convoluting the LED or 1-sun spectrum to an impulse response of the photoactive layer, and these values were then translated into the respective current densities. Unfortunately, the ideal current density did not involve the EQE and resistive effects that occurred at the interface and electrode contact points.

Results and discussion

Figure 1(a) depicts the electrical properties (carrier concentration [cm^{-3}], electrical resistivity [$\Omega\cdot\text{cm}^2$], and Hall mobility [$\text{cm}^2\cdot\text{V}^{-1}\cdot\text{s}^{-1}$]) of the ALD-processed SnO_2 films, determined via Hall measurements, as functions of the growth temperature. The film resistivity decreased drastically with an increasing growth temperature, from $113 \Omega\cdot\text{cm}$ at 100°C to $1.6 \times 10^{-3} \Omega\cdot\text{cm}$ at 250°C . These resistivity values were slightly lower than those of the previous ALD-synthesized SnO_2 thin films prepared using different precursors^{22–24} and were comparable to those of PVD-fabricated SnO_2 thin films^{25,26}. A significant increase in the carrier concentration, from $2.2 \times 10^{15} \text{ cm}^{-3}$ to $7.3 \times 10^{20} \text{ cm}^{-3}$, was observed as the growth temperature was increased from 100°C to 250°C . An inverse U-shape (100 – 150°C : steep reduction; 150 – 200°C : slight decrease; and 200 – 250°C : moderate increase) was observed in the evolution of the Hall mobility with an increasing temperature. Based on these observations, the reduction in the resistivity of the SnO_2 thin films was attributed to the increase in carrier concentration. The sheet resistance (R_{SH}) values are shown in Fig. 1(b). The R_{SH} of the 150-nm-thick SnO_2 film deposited at 250°C was the lowest, with a value of $\sim 98 \Omega\cdot\text{sq}^{-1}$. Hence, a deposition temperature of 250°C was considered optimal for producing TCE layers with good performance. The acceptable electrical properties of the SnO_2 thin films prepared using $\text{N,N}'$ -tert-butyl-1,1-dimethylethylenediamine stannylene and ozone suggest that they can be suitable alternatives to ITO.

To verify the origin of the electrical properties of the SnO_2 thin films, the compositions and crystal structures of the films prepared at different growth temperatures were compared. All the samples were 150 nm thick. Stoichiometric analysis of the SnO_2 thin films was

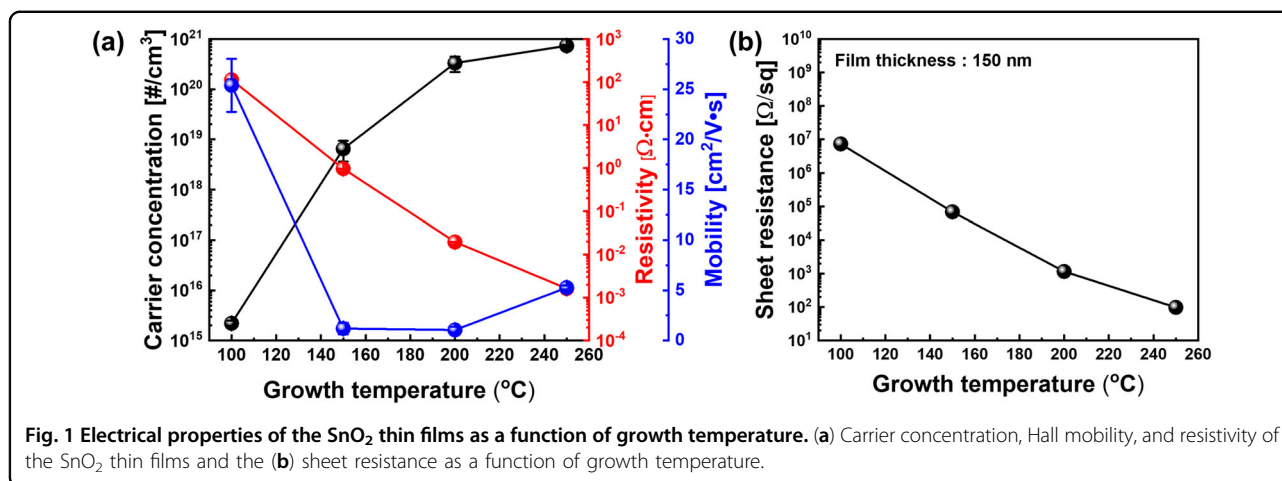


Fig. 1 Electrical properties of the SnO₂ thin films as a function of growth temperature. (a) Carrier concentration, Hall mobility, and resistivity of the SnO₂ thin films and the (b) sheet resistance as a function of growth temperature.

Table 1 Temperature dependence of the O/Sn atomic ratios in the SnO₂ thin films, as determined by XPS.

Deposition temperature (°C)	100	150	200	250
O/Sn ratio	1.70	1.68	1.60	1.54

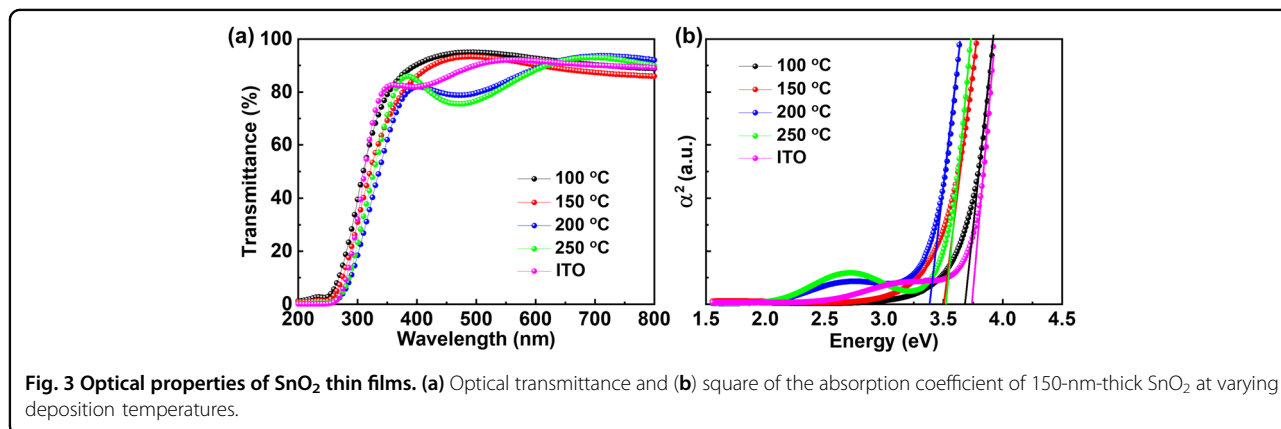
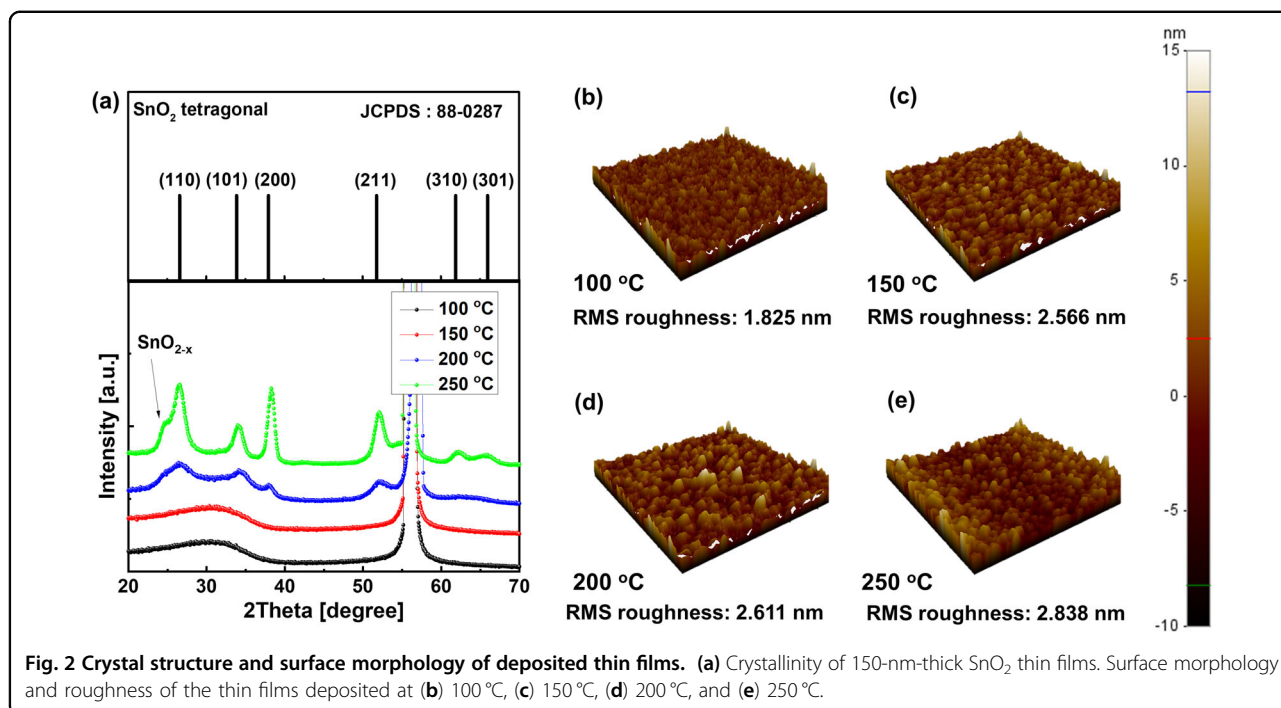
performed by depositing the films on silicon (100) substrates and analyzing them via X-ray photoelectron spectroscopy (XPS) (Table 1).

We observed that the O/Sn ratio gradually decreased with an increasing growth temperature. Regarding n-type oxide materials, the oxygen deficiency resulted in oxygen vacancies that acted as electron donors, which were the origins of the electron carriers²⁷. The oxygen deficiency, and hence, carrier concentration, increased with an increasing growth temperature. Furthermore, the carrier mobility decreased significantly at 100 °C, which was attributed to scattering between the carriers. At 250 °C, the mobility increased from $\sim 1 \text{ cm}^2 \cdot \text{V}^{-1} \cdot \text{s}^{-1}$ to $5.3 \text{ cm}^2 \cdot \text{V}^{-1} \cdot \text{s}^{-1}$, despite the high carrier concentration, compared to those at 150 °C and 200 °C.

The crystallinity of the SnO₂ films was investigated via X-ray diffraction (XRD). Figure 2(a) depicts the diffraction patterns of the thin films deposited at growth temperatures between 100 °C and 250 °C. XRD analysis revealed the formation of amorphous SnO₂ at 100 °C and 150 °C and polycrystalline tetragonal SnO₂ (JCPDS: 88-0287) above 200 °C. Typical diffraction patterns of the tetragonal SnO₂ phase were observed, along with satellite peaks around the SnO₂ (110) peak, which implied the presence of nonstoichiometric SnO_{2-x} phases²⁸ and was consistent with the XPS-determined atomic concentration ratios. The observed trends in the Hall mobility can be explained by the thin film crystallinity. At low growth temperatures, scattering between carriers occurred owing to the

amorphous films, thereby resulting in decreased mobility; however, the highly crystalline films that were prepared at higher temperatures typically showed lower carrier scattering at the grain boundaries. The crystallization of SnO₂ can result in an increase in transitions to unoccupied states at the bottom of the conduction band through the formation of SnO₆ octahedral structures¹². As a result, we observed increased carrier mobility at 250 °C, despite the high carrier concentration.

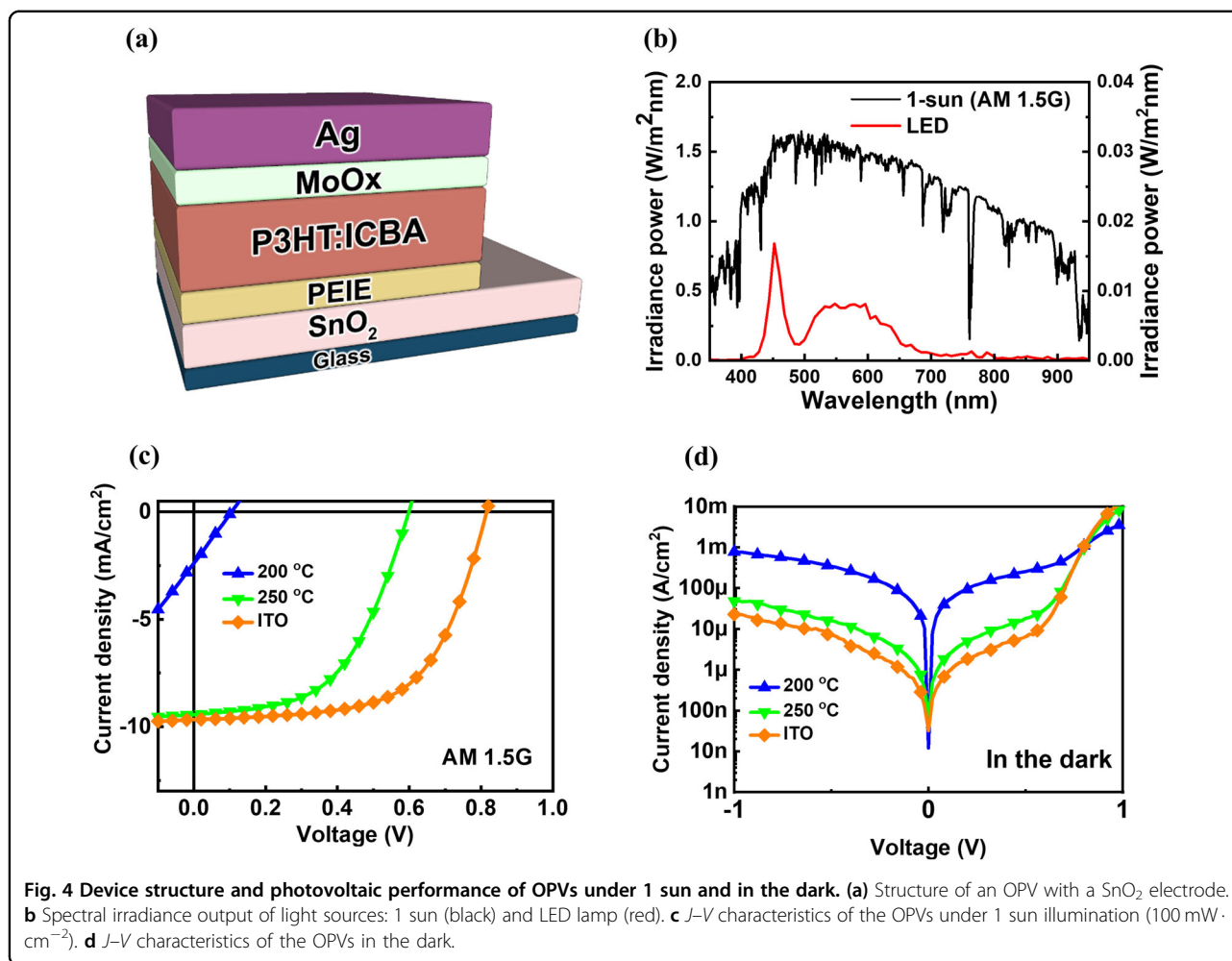
The surface morphology and roughness of the thin films are shown in Fig. 2(b)–(e). During grain growth, the roughness of the SnO₂ thin films increased from 1.8 nm to 2.8 nm. Notably, the reference ITO substrates showed a roughness value of 2.2 nm. However, the roughness was <2 % of the film thickness, resulting in a uniform and smooth surface that could minimize surface light scattering when applied to OPV devices. Figure 3(a) and (b) show the optical transmittance and bandgap analysis results, respectively, which were plotted using the Tauc plot method²⁹. The SnO₂ films deposited at 100 °C and 150 °C showed higher transmittance than ITO. However, the SnO₂ films deposited at 200 °C and 250 °C had lower transmittance than ITO, which is attributed to photon scattering at the grain boundaries of the crystalline films. This result, along with the light absorbed by donor states in the lower energy levels of the bandgap, resulted in a decrease in transmittance in the absorption-edge region. Although some of the SnO₂ films had lower transmittance than ITO, the observed transmittance of these SnO₂ films was considered to be sufficient for their use as TCE layers. The optical bandgap shown in Fig. 3(b) decreased with an increasing growth temperature, up to 200 °C, and then increased again at 250 °C. The decrease in the bandgap in the 100–200 °C region may be due to the decrease in the number of tin ions. The reported bandgaps of SnO and SnO₂ were 2.5–3.0 eV and 3.6 eV, respectively³⁰. When the O/Sn ratio decreased, the number of Sn²⁺ increased, which tended to decrease the optical bandgap³⁰. The bandgap for SnO₂



deposited at 250 °C could not be explained by the presence of Sn²⁺; however, it may be a result of the Burstein–Moss effect³¹, wherein the optical bandgap of a degenerated semiconductor shifts to a higher energy level due to a degenerate state. The Hall measurement results (Fig. 1(a)) showed that SnO₂ deposited at 250 °C had the highest carrier concentration among all samples and could be considered a degenerated conductor³² that induced a blueshift in the optical bandgap. However, the overall bandgaps of the SnO₂ thin films were smaller than that of ITO. Although wider optical bandgaps are favorable for TCE layers, an SnO₂ TCE layer may improve the OPV efficiency, depending on several optical parameters.

To evaluate the photovoltaic performance of OPVs with SnO₂-based TCEs, OPVs with SnO₂/ethoxylated

polyethyleneimine (PEIE)/P3HT:ICBA/MoO_x/Ag structures were fabricated. An inverted structure was employed to avoid the use of reactive and acidic components and to ensure improved stability in air compared to conventional structures³³. Figure 4(a) shows a schematic illustration of the device architecture. The WF values of the SnO₂ films were measured using a Kelvin probe. The reference ITO TCE and the SnO₂ TCE showed WF values of ~4.7 eV and ~4.6 eV, respectively. Although the WF values of the SnO₂ films were lower than that of the reference ITO TCE, they did not seem to be low enough to provide an effective energy-level alignment with the electron affinity (EA) of the electron-acceptor material ICBA. Therefore, a polymeric surface modification with PEIE was performed to further



lower the WF value. The simple aliphatic amine group in this polymer, which has electron donating properties, induced a dipole moment at the conductor surface by lowering the electrostatic potential, resulting in a decrease in the WF of the conductor surface³³. The PEIE-modified SnO₂ and PEIE-modified ITO TCEs had WF values of ~3.9 eV and ~4.0 eV, respectively, which are expected to satisfy the energy-level alignment with the EA of ICBA.

First, the photovoltaic performances of the OPVs with the two types of TCEs, namely, ITO and SnO₂ (growth temperatures: 100 °C, 150 °C, 200 °C, and 250 °C), were evaluated under 1 sun illumination ($I_L = 100 \text{ mW} \cdot \text{cm}^{-2}$). Hereafter, the OPV samples with the ITO TCE are referred to as the “reference” samples, whereas those prepared using the Sn₂O films are referred to as TO250, with the numerical value indicating the growth temperature. The output spectra obtained under 1 sun illumination, for simulating outdoor conditions, and an LED lamp, for simulating indoor conditions, are shown in Fig. 4(b). In addition, Fig. 4(c) shows the current density–voltage (*J-V*)

characteristics of the OPVs under 1 sun illumination, where the photovoltaic parameters are averaged for 10 devices, as summarized in Table 2. The OPVs with the SnO₂ films (TO100, TO150, and TO200) showed no activity under 1 sun illumination. This result is attributed to their poor electrical properties, such as the relatively high R_{SH} of the SnO₂ TCE. High R_{SH} values can result in OPVs with high series resistance (R_s), thereby inducing poor photovoltaic performance with a lowered short-circuit current density (J_{SC}) and a reduced fill factor (FF). The TO250 OPV system showed a PCE of $2.4 \pm 0.4\%$, with an open-circuit voltage (V_{OC}) of $532 \pm 52 \text{ mV}$, a J_{SC} of $9.9 \pm 0.4 \text{ mA} \cdot \text{cm}^{-2}$, and an FF of $45.9 \pm 0.4\%$. In comparison, the reference OPV system showed reasonable photovoltaic performance with a V_{OC} of $744 \pm 11 \text{ mV}$, a J_{SC} of $9.9 \pm 0.4 \text{ mA} \cdot \text{cm}^{-2}$, and an FF of $57.1 \pm 4.7\%$, yielding a PCE of $4.2 \pm 0.5\%$. Figure 4(d) shows the semi-log *J-V* curves of the OPV systems obtained in the dark. The TO250 OPV showed comparable performance in the dark, with a low current density compared to the reference system, indicating its potential as a TCE for indoor applications.

Table 2 Averaged photovoltaic parameters of the OPVs under 1 sun illumination.

TCE	V_{OC} (mV)	J_{SC} ($\text{mA} \cdot \text{cm}^{-2}$)	FF (%)	PCE (%) (Max PCE)	R_{pA} ($\Omega \cdot \text{cm}^2$)	R_{sA} ($\Omega \cdot \text{cm}^2$)
TO100	49 ± 13	0.0 ± 0.0	23.4 ± 1.1	0.0 ± 0.0 (0)	$(5.8 \pm 4.2) \times 10^3$	3970 ± 2291
TO150	19 ± 12	0.0 ± 0.0	10.3 ± 14.6	0.0 ± 0.0 (0)	$(4.9 \pm 2.6) \times 10^2$	372 ± 147
TO200	100 ± 21	1.9 ± 0.5	25.0 ± 0.8	0.0 ± 0.0 (0)	$(5.0 \pm 0.9) \times 10$	52 ± 10
TO250	532 ± 52	9.9 ± 0.4	45.9 ± 2.1	2.4 ± 0.4 (2.8)	$(4.2 \pm 1.3) \times 10^2$	14 ± 1
ITO reference	744 ± 11	9.9 ± 0.4	57.1 ± 4.7	4.2 ± 0.5 (4.7)	$(8.5 \pm 1.6) \times 10^2$	13 ± 11

Circuit models are often used to model electrochemical systems and provide insights into the results. An OPV system can be modeled with a single diode-based equivalent circuit (Fig. S2). It is comprised of a current source parallel to an ideal diode and two parasitic resistances: R_S and shunt resistance (R_P). The photocurrent density (J_{ph}) generated during illumination is modeled by a constant current source. The equivalent circuit can be solved analytically by using the Shockley equation to determine J_{SC} and V_{OC} ³⁴:

$$J_{sc} = -\frac{1}{1 + \frac{R_S}{R_P}} \left\{ J_{ph} - J_o \left(\exp \left(\frac{|J_{sc}| R_S A}{nkT} \right) - 1 \right) \right\} \quad (1)$$

$$V_{OC} = n \frac{kT}{e} \ln \left\{ 1 + \frac{J_{ph}}{J_o} \left(1 - \frac{V_{OC}}{J_{ph} R_P A} \right) \right\} \quad (2)$$

where J_{ph} is the photogenerated current density, J_o is the reverse saturation current density, e is the fundamental charge of an electron, n is the ideality factor, T is the temperature, k is Boltzmann's constant ($8.617 \times 10^{-5} \text{ eV} \cdot \text{K}^{-1}$), and A is the active area of the device. In this study, R_{sA} and R_{pA} values were estimated from the inverse slopes of the characteristic J - V curves under illumination at 0.98–1.0 V and near the J_{SC} point, respectively.

The identical J_{SC} values of the TO250 and reference OPV devices under 1 sun illumination were due to their similar R_{sA} values ($14 \Omega \cdot \text{cm}^2$ and $13 \Omega \cdot \text{cm}^2$, respectively) and optoelectrical properties. It can be seen from Eq. (1) that J_{SC} was significantly dependent on R_{sA} and decreased approximately exponentially with increasing R_{sA} values. However, as similar R_{sA} values were observed for the devices with both types of TCEs, no significant difference in the J_{SC} values was expected. Moreover, similar EQE spectra (Fig. 5(a)) for both TCEs in the spectral range of 300–700 nm indicated similar J_{SC} values in both cases.

The different V_{OC} values of the two devices (532 ± 52 mV for TO250 and 744 ± 11 mV for the reference OPVs) were due to their different R_{SH} values. In general, high recombination rates, compared to the drifting of charge carriers in TCEs, result in higher R_{SH} values³⁵. An increase in the leakage current resulted in lower R_{pA}

values (SnO_2 : $420 \Omega \cdot \text{cm}^2$ and ITO: $850 \Omega \cdot \text{cm}^2$). From Eq. (2), it can be inferred that the low R_{pA} values of the SnO_2 -based OPVs resulted in the observed low V_{OC} values and is also the reason for the observed low dark current and high EQE of the devices. The reference OPV system did not suffer a comparable loss in voltage because of the lower R_{SH} of ITO ($\sim 10 \Omega \cdot \text{sq}^{-1}$), confirming its superior performance under 1 sun illumination.

The indoor performance of the SnO_2 -based OPV systems under low light conditions (an LED of 1000 lx) differed from that under 1 sun illumination. A comparison of the J - V curves of the OPV systems under a 1000 lx LED source ($I_L = 0.28 \text{ mW} \cdot \text{cm}^{-2}$) is shown in Fig. 5(b). The average indoor photovoltaic parameters for 10 devices under LED illumination are summarized in Table 3. The reference OPV systems had a V_{OC} of 640 ± 3 mV, a J_{SC} of $83.4 \pm 4.3 \mu\text{A} \cdot \text{cm}^{-2}$, and an FF of $70.0 \pm 1.3\%$, resulting in a PCE of $13.3 \pm 0.8\%$ under 1000 lx LED illumination. Interestingly, the TO200 OPV systems that barely operated under 1 sun illumination showed comparable photovoltaic performance with a PCE of $11.7 \pm 0.1\%$, a V_{OC} of 603 ± 8 mV, a J_{SC} of $80.1 \pm 1.9 \mu\text{A} \cdot \text{cm}^{-2}$, and an FF of $67.6 \pm 1.4\%$. Moreover, the TO250 sample showed a slightly higher PCE of $14.6 \pm 0.3\%$, compared to that of the reference OPVs, with a V_{OC} of 660 ± 3 mV, a J_{SC} of $87.1 \pm 2.2 \mu\text{A} \cdot \text{cm}^{-2}$, and an FF of $71.2 \pm 0.8\%$.

The similar measured J_{SC} values for the SnO_2 -based OPVs (TO200 and TO250) and the reference system clearly indicated that J_{SC} was not highly dependent on the R_{SH} of the TCEs (which varied significantly depending on the TCE type). Under low-light indoor conditions, the low generated J_{ph} could easily flow through R_S , resulting in similar J_{SC} values, despite the difference in the R_{SH} values of the TCEs. To further investigate the J_{SC} values, power absorption ratios were calculated by finite-difference time-domain (FDTD) simulations. Figure S3 shows the light penetration profile at a wavelength of 450 nm, whereas Fig. 5(c) shows the power absorption ratios over the output spectral region of the LED lamp (400–700 nm). Similar to the transmittance data discussed above, comparable power absorption ratios were observed for the devices with the SnO_2 TCEs (TO200 and TO250), whereas the reference device showed a slight

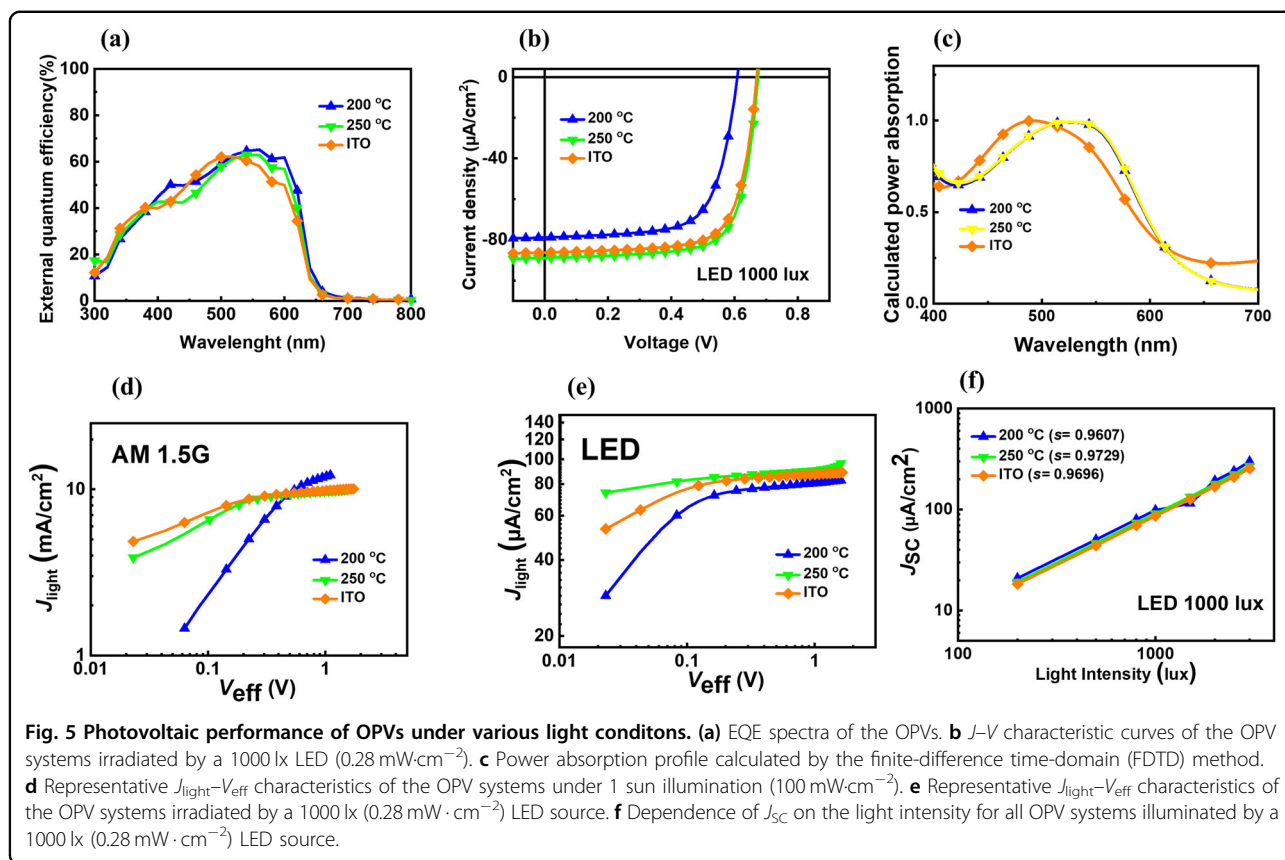


Table 3 Averaged photovoltaic parameters of the OPVs under an LED source (1000 lx).

TCE	V_{OC} (mV)	J_{SC} ($\mu\text{A}\cdot\text{cm}^{-2}$)	FF (%)	PCE (%) (Max PCE)	R_{pA} ($\Omega\cdot\text{cm}^2$)	R_{SA} ($\Omega\cdot\text{cm}^2$)	P_{max} ($\mu\text{W}\cdot\text{cm}^{-2}$)
TO100	50 ± 23	0.1 ± 0.1	19.9 ± 8.2	0.0 ± 0.0 (0)	$(3.9 \pm 0.4) \times 10^5$	202539 ± 8992	0.0 ± 0.0
TO150	67 ± 20	8.1 ± 1.8	24.4 ± 0.3	0.0 ± 0.0 (0)	$(8.0 \pm 0.5) \times 10^3$	6704 ± 1338	0.1 ± 0.1
TO200	603 ± 8	80.1 ± 1.9	67.6 ± 1.4	11.7 ± 0.1 (11.8)	$(1.3 \pm 0.2) \times 10^5$	235 ± 29	32.6 ± 0.4
TO250	660 ± 3	87.1 ± 2.2	71.2 ± 0.8	14.6 ± 0.3 (14.9)	$(1.5 \pm 0.4) \times 10^5$	28 ± 1	40.9 ± 0.8
ITO reference	640 ± 3	83.4 ± 4.3	70.0 ± 1.3	13.3 ± 0.8 (14.1)	$(1.3 \pm 0.4) \times 10^5$	27 ± 2	37.4 ± 2.1

blueshift in the absorption spectrum. For a more quantitative analysis, the maximum achievable J_{SC} values were extracted by multiplying the power absorption ratios by the spectral irradiance of the LED lamp (Table S1). Notably, the FDTD simulation of the J_{SC} values included only optical effects (not electrical effects). Interestingly, the calculation showed lower J_{SC} values for the reference OPVs than those of the TO200 and TO250 devices, wherein TO200 showed the highest value. These results indicated that for high indoor performance, TCEs with good electrical conductivity were required, despite the tolerance of the device to the R_{SH} of the TCE under low-light conditions. Notably, the TO100 and TO150 films were ineffective TCEs, resulting in poor device performance due to their remarkably high R_{SH} values.

Remarkably, under the 1000 lx LED lamp, the highest V_{OC} was obtained from the TO250 device, even though it showed extremely poor performance under 1 sun illumination. Before we discuss the high V_{OC} value of the TO250 device under indoor light conditions, it is important to understand the limit of the OPV V_{OC} . The V_{OC} of OPVs is known to be limited by the WF difference between the hole-collecting electrode (HCE) and the electron-collecting electrode (ECE) or the energy level difference between the EA of the acceptor material and the ionization potential energy (IE) of the donor material, namely, the carrier density limit. If the WF of the ECE is deeper (from the vacuum level) than the EA of the acceptor and the WF of the HCE is shallower than the IE

of the donor, then the V_{OC} is likely to be limited to the WF difference between the ECE and HCE. In contrast, when the ECE possesses a lower WF value than the EA of the acceptor and the HCE shows a larger WF value than the IE of the donor, the V_{OC} is limited to the energy level difference between the EA of the acceptor and the IE of the donor. Our results can be explained by the WF difference. Moreover, under indoor light conditions, the OPVs with SnO₂ TCEs were considerably insensitive to the high R_{SH} of the TCEs; hence, the low V_{OC} value of the TO250 device under 1 sun illumination was not expected. The EA of the ICBA acceptor was ~3.5 eV, and the WF values (measured with a Kelvin probe) of the two ECEs, namely, SnO₂/PEIE and the reference ITO/PEIE, were ~3.8 eV and ~4.0 eV, respectively³⁶. As the WF values of the two ECEs were lower than the EA of the ICBA, the V_{OC} difference between the TO250 device and reference OPVs was probably due to the different WF values of the ECEs. That is, under illumination, quasi-Fermi levels could have formed above the WF levels in the acceptor material, where the WF levels of the ECEs could limit the V_{OC} , thereby resulting in the observed V_{OC} difference.

The variation in the FF values is explained by analyzing the equivalent circuit model, where $FF = [J_{max} \times V_{max}] / [J_{SC} \times V_{OC}]$. In this relationship, the following parameters were normalized: V_{OC} ($v_{OC} = eV_{OC} / nkT$), R_S ($r_S = R_S / R_{CH}$), and R_P ($r_P = R_P / R_{CH}$). The characteristic resistance was defined as $R_{CH} = (V_{OC} / J_{SC} \times A)$; therefore, the FF combined the effects of r_S and r_P :

$$FF = \left\{ \frac{v_{OC} - \ln(v_{OC} + 0.72)}{v_{OC} + 1} \right\} (1 - 1.1r_S) + 0.19r_S^2 \times \left\{ 1 - \frac{(v_{OC} + 0.7)}{v_{OC}} \frac{\left\{ \frac{v_{OC} - \ln(v_{OC} + 0.72)}{v_{OC} + 1} \right\} (1 - 1.1r_S) + 0.19r_S^2}{r_P} \right\} \times \left(0 \leq r_S + \frac{1}{r_P} \leq 0.4 \right) \quad (3)$$

Based on the previous observations that $J_{SC} \propto$ light intensity and $V_{OC} \propto \log$ (light intensity), it was assumed that higher R_{CH} values could be attained under indoor conditions than under 1 sun illumination. In addition, compared to R_P and R_{CH} , the R_S was low; thus, R_S had a negligible effect on the indoor performance of the devices. Due to the high R_{CH} values, the r_S of the devices (TO250: 0.0037 and reference: 0.0035) were low and had an insignificant effect on their FFs. However, sufficiently high r_P values (TO250: 19.7 and reference: 16.9) contributed to maximizing the FF under indoor conditions.

To evaluate the charge generation and collection process, the light-induced current density (J_{light}) was plotted against the effective voltage (V_{eff}). J_{light} is the difference in the current densities under illumination and in the dark, whereas V_{eff} is the difference between the voltages at $J_{PH} = 0$ and the applied

voltage³⁷. Figure 5(d) shows the $J_{light} - V_{eff}$ characteristics of the devices under 1 sun illumination. A fast J_{light} saturation was observed for the reference OPV at a V_{eff} of 0.31 V, indicating effective charge transport and collection, whereas the TO200 and TO250 OPVs saturated at higher V_{eff} values of 0.439 and 1.2 V, respectively. Relatively poor charge generation/collection in the SnO₂-based OPV systems resulted in low FF values under 1 sun illumination. Under 1000 lx LED illumination, the J_{light} saturation of SnO₂- and ITO-based OPV systems occurred at similar V_{eff} values of ~0.172 and 0.167 V, respectively, demonstrating effective charge carrier generation/extraction with negligible trapping (Fig. 5(e)). To understand the charge carrier recombination behavior in the OPV systems, J_{SC} was derived as a function of light intensity (Fig. 5(f)). J_{SC} is related to light intensity (I_{light}) by a power law relationship ($J_{SC} \propto I_{light}^s$), where s is the recombination rate (0.75–1) and can be obtained by linear fitting of the data. An s value close to one indicates that weak bimolecular recombination is the dominant recombination mechanism in bulk-heterojunction OPV systems. In our study, all devices showed s values close to one (TO250: 0.972, and ITO TCE: 0.969), indicating that the same recombination mechanism was dominant in our devices.

Conclusions

We evaluated the indoor performance of OPV systems with ALD-synthesized SnO₂ TCEs. The thicknesses of the SnO₂ layers were precisely controlled during the ALD process to produce uniform and smooth films at a low temperature. Under 1 sun illumination, the OPV systems with SnO₂ TCEs, which had higher R_{SH} values, showed poorer performance than the devices with ITO TCEs. However, under LED illumination, the devices with SnO₂ TCEs showed acceptable indoor performance, with only slightly lower PCE values than that of the reference device. We verified that the performance of the OPV system with the SnO₂ TCE depended on R_P instead of R_S due to the low photocurrent generated at the low-light intensities under indoor conditions. Overall, the SnO₂ TCEs showed indoor performance similar to that of commercial ITO TCEs. In addition, their lower cost could substantially reduce the total cost of indoor OPV systems, making them promising candidates for future indoor energy harvesting applications.

Acknowledgements

This research was supported by the Technology Development Program to Solve Climate Changes of the National Research Foundation of Korea, which is funded by the Ministry of Science, ICT & Future Planning (NRF-2016M1A2A2940912) and the Technology Innovation Program (20011336) funded by the Ministry of Trade, Industry & Energy, Korea. In addition, this work was supported by Samsung Electronics Co., Ltd. (IO201217-08221-01). Finally, this work was supported by the Brain Korea 21 FOUR Project in 2021.

Author details

¹Division of Materials Science and Engineering, Hanyang University, Seoul, Republic of Korea. ²Division of Electronics and Electrical Engineering, Dongguk University, Seoul, Republic of Korea. ³School of Electrical Engineering, Korea

University, Seoul, Republic of Korea. ⁴Division of Nanoscale Semiconductor Engineering, Hanyang University, Seoul, Republic of Korea. ⁵Department of Energy and Materials Engineering, Dongguk University, Seoul, Republic of Korea

Author contributions

The paper was written through contributions of all authors. All authors have given approval to the final version of the manuscript.

Conflict of interest

The authors declare no competing interests.

Publisher's note

Springer Nature remains neutral with regard to jurisdictional claims in published maps and institutional affiliations.

Supplementary information The online version contains supplementary material available at <https://doi.org/10.1038/s41427-021-00310-2>.

Received: 25 January 2021 Revised: 9 March 2021 Accepted: 29 March 2021.

Published online: 7 May 2021

References

- Freitag, M. et al. Dye-sensitized solar cells for efficient power generation under ambient lighting. *Nat. Photon.* **11**, 372–378 (2017).
- Cutting, C. L., Bag, M. & Venkataraman, D. Indoor light recycling: a new home for organic photovoltaics. *J. Mater. Chem.* **C4**, 10367–10370 (2016).
- Li, G., Zhu, R. & Yang, Y. Polymer solar cells. *Nat. Photon.* **6**, 153–161 (2012).
- Inganäs, O. Organic photovoltaics over three decades. *Adv. Mater.* **30**, e1800388 (2018).
- Lee, H. K. H. et al. Organic photovoltaic cells – promising indoor light harvesters for self-sustainable electronics. *J. Mater. Chem. A* **6**, 5618–5626 (2018).
- Hong, L. et al. Eco-compatible solvent-processed organic photovoltaic cells with over 16% efficiency. *Adv. Mater.* **31**, e1903441 (2019).
- Cui, Y. et al. Efficient semitransparent organic solar cells with tunable color enabled by an ultralow-bandgap nonfullerene acceptor. *Adv. Mater.* **29**, 1703080 (2017).
- Shafian, S., Son, J., Kim, Y., Hyun, J. K. & Kim, K. Active-material-independent color-tunable semitransparent organic solar cells. *ACS Appl. Mater. Interfaces* **11**, 18887–18895 (2019).
- Kim, S., Jahandar, M., Jeong, J. H. & Lim, D. C. Recent progress in solar cell technology for low-light indoor applications. *Curr. Altern. Energy* **2**, 1–15 (2018).
- Steim, R. et al. Organic photovoltaics for low light applications. *Sol. Energy Mater. Sol. Cells* **95**, 3256–3261 (2011).
- Kippelen, B. & Brédas, J.-L. Organic photovoltaics. *Energy Environ. Sci.* **2**, 251–261 (2009).
- Choi, D.-W., Maeng, W. J. & Park, J.-S. The conducting tin oxide thin films deposited via atomic layer deposition using tetrakis-dimethylamino tin and peroxide for transparent flexible electronics. *Appl. Surf. Sci.* **313**, 585–590 (2014).
- Ngamsinlapasathian, S., Sreethawong, T., Suzuki, Y. & Yoshikawa, S. Doubled layered ITO/SnO₂ conducting glass for substrate of dye-sensitized solar cells. *Sol. Energy Mater. Sol. Cells* **90**, 2129–2140 (2006).
- Goo, J. S., Lee, J.-H., Shin, S.-C., Park, J.-S. & Shim, J. W. Undoped ZnO electrodes for low-cost indoor organic photovoltaics. *J. Mater. Chem. A* **6**, 23464–23472 (2018).
- Thangaraju, B. Structural and electrical studies on highly conducting spray deposited fluorine and antimony doped SnO₂ thin films from SnCl₂ precursor. *Thin Solid Films* **402**, 71–78 (2002).
- Kim, H., Auyeung, R. C. Y. & Piqué, A. Transparent conducting F-doped SnO₂ thin films grown by pulsed laser deposition. *Thin Solid Films* **516**, 5052–5056 (2008).
- Stefik, M. et al. Transparent, conducting Nb:SnO₂ for host–guest photoelectrochemistry. *Nano Lett.* **12**, 5431–5435 (2012).
- Vaufrey, D. et al. Reactive ion etching of sol–gel-processed SnO₂ transparent conducting oxide as a new material for organic light emitting diodes. *Synth. Met.* **127**, 207–211 (2002).
- Kim, H. & Piqué, A. Transparent conducting Sb-doped SnO₂ thin films grown by pulsed-laser deposition. *Appl. Phys. Lett.* **84**, 218–220 (2004).
- Ruske, M., Bräuer, G., Pistner, J., Pfäfflin, U. & Szczyrbowski, J. Properties of SnO₂ films prepared by DC and MF reactive sputtering. *Thin Solid Films* **351**, 146–150 (1999).
- Khan, A. F., Mehmood, M., Rana, A. M. & Bhatti, M. T. Effect of annealing on electrical resistivity of rf-magnetron sputtered nanostructured SnO₂ thin films. *Appl. Surf. Sci.* **255**, 8562–8565 (2009).
- Heo, J., Hock, A. S. & Gordon, R. G. Low temperature atomic layer deposition of tin oxide. *Chem. Mater.* **22**, 4964–4973 (2010).
- Heo, J., Kim, S. B. & Gordon, R. G. Atomic layer deposition of tin oxide with nitric oxide as an oxidant gas. *J. Mater. Chem.* **22**, 4599–4602 (2012).
- Lee, B. K. et al. An, Physical/chemical properties of tin oxide thin film transistors prepared using plasma-enhanced atomic layer deposition. *Mater. Res. Bull.* **47**, 3052–3055 (2012).
- Korotchenkov, G., Brynzari, V. & Dmitriev, S. Electrical behavior of SnO₂ thin films in humid atmosphere. *Sens. Actuators B* **54**, 197–201 (1999).
- Edwards, P. P., Porch, A., Jones, M. O., Morgan, D. V. & Perks, R. M. Basic materials physics of transparent conducting oxides. *Dalton Trans.* **19**, 2995–3002 (2004).
- Nomura, K. et al. Room-temperature fabrication of transparent flexible thin-film transistors using amorphous oxide semiconductors. *Nature* **432**, 488–492 (2004).
- Pan, J., Wang, L., Yu, J. C., Liu, G. & Cheng, H.-M. A nonstoichiometric SnO_{2-δ} nanocrystal-based counter electrode for remarkably improving the performance of dye-sensitized solar cells. *Chem. Commun.* **50**, 7020–7023 (2014).
- Tauc, J., Grigorovici, R. & Vancu, A. Optical properties and electronic structure of amorphous germanium. *Phys. Stat. Solidi B* **15**, 627–637 (1966).
- Wang, C.-H., Chen, S.-W., Wu, J.-M., Wei, C.-N. & Bor, H.-Y. Effect of post-deposition oxidation and subsequent reduction annealing on electric and optical properties of amorphous ZnO–SnO₂ transparent conducting films. *Electrochem. Solid-State Lett.* **14**, P5 (2010).
- Ziabari, A. A. & Rozati, S. Carrier transport and bandgap shift in n-type degenerate ZnO thin films: the effect of band edge nonparabolicity. *Phys. B: Cond. Matt.* **407**, 4512–4517 (2012).
- Takagi, A. et al. Carrier transport and electronic structure in amorphous oxide semiconductor, a-InGaZnO₄. *Thin Solid Films* **486**, 38–41 (2005).
- Zhou, Y. et al. A universal method to produce low-work function electrodes for organic electronics. *Science* **336**, 327–332 (2012).
- Yoo, S., Domesq, B. & Kippelen, B. Intensity-dependent equivalent circuit parameters of organic solar cells based on pentacene and C60. *J. Appl. Phys.* **97**, 103706 (2005).
- Park, S. Y. et al. Alkoxybenzothiadiazole-based fullerene and nonfullerene polymer solar cells with high shunt resistance for indoor photovoltaic applications. *ACS Appl. Mater. Interfaces* **10**, 3885–3894 (2018).
- Mihailetchi, V. D., Blom, P. W. M., Hummelen, J. C. & Rispen, M. T. Cathode dependence of the open-circuit voltage of polymer: fullerene bulk hetero-junction solar cells. *J. Appl. Phys.* **94**, 6849–6854 (2003).
- You, Y. J. et al. Highly efficient indoor organic photovoltaics with spectrally matched fluorinated phenylene-alkoxybenzothiadiazole-based wide bandgap polymers. *Adv. Funct. Mater.* **29**, 1901171 (2019).